

Submitted to the Astrophysical Journal

Neon and Oxygen Abundances in M33

Nathan R. Crockett

Steward Observatory, University of Arizona, Tucson, AZ 85721,

and National Optical Astronomy Observatories, 950 N. Cherry Avenue, Tucson, AZ 85719

`crockett@noao.edu`

Donald R. Garnett

Steward Observatory, University of Arizona

933 N. Cherry Avenue, Tucson, AZ 85721

`dgarnett@as.arizona.edu`

Philip Massey¹

Lowell Observatory

1400 W. Mars Hill Road, Flagstaff, AZ 86001

`massey@lowell.edu`

and

George Jacoby¹

WIYN Observatory

950 N. Cherry Avenue, Tucson, AZ 85719

`jacoby@noao.edu`

ABSTRACT

We present new spectroscopic observations of 13 H II regions in the Local Group spiral galaxy M33. The regions observed range from 1 to 7 kpc in distance from the nucleus. Of the 13 H II regions observed, the [O III] $\lambda 4363$ line was detected in six regions.

¹Visiting Astronomer, Kitt Peak National Observatory, National Optical Astronomy Observatories, which is operated by the Association of Universities for Research in Astronomy, Inc. (AURA) under cooperative agreement with the National Science Foundation.

Electron temperatures were thus able to be determined directly from the spectra using the [O III] $\lambda\lambda 4959, 5007/\lambda 4363$ line ratio. Based on these temperature measurements, oxygen and neon abundances and their radial gradients were calculated. For neon, a gradient of -0.016 ± 0.017 dex/kpc was computed, which agrees with the Ne/H gradient derived previously from ISO spectra. A gradient of -0.012 ± 0.011 dex/kpc was computed for O/H, much shallower than was derived in previous studies. The newly calculated O/H and Ne/H gradients are in much better agreement with each other, as expected from predictions of stellar nucleosynthesis. We examine the correlation between the WC/WN ratio and metallicity, and find that the new M33 abundances do not impact the observed correlation significantly. We also identify two new He II-emitting H II regions in M33, the first to be discovered in a spiral galaxy other than the Milky Way. In both cases the nebular He II emission is not associated with Wolf-Rayet stars. Therefore, caution is warranted in interpreting the relationship between nebular He II emission and Wolf-Rayet stars when both are observed in the integrated spectrum of an H II region.

Subject headings: galaxies:abundances – galaxies:individual(M33) – galaxies: ISM – galaxies: Local Group – galaxies: spiral

1. Introduction

Spectroscopic observations of emission lines in H II regions is still a primary source of information of element abundances in the interstellar medium of spiral and irregular galaxies. In the metal-rich inner disks of spirals, however, abundances derived from such measurements have had considerable uncertainty. The main reason for this has been the lack of accurate electron temperature estimates, T_e . The reason T_e estimates have remained uncertain for so long is largely due to the fact that the auroral lines on which accurate temperature estimates rely (e.g. [O III] $\lambda 4363$, [N II] $\lambda 5755$, and [S III] $\lambda 6312$), are intrinsically weak and thus difficult to detect. This difficulty is compounded in high metallicity H II regions ($\gtrsim 0.5 (O/H)_\odot$) because of increased cooling via IR fine structure lines, which reduces the electron temperature and makes the temperature-sensitive diagnostic line ratios even more difficult to measure.

In the absence of direct temperature measurements, past studies of the composition of H II regions in spirals have made use of derived relations between O/H and a strong emission line ratio, such as $R_{23} = ([O II]\lambda 3727 + [O III]\lambda\lambda 4959, 5007)/H\beta$, with the relation often “calibrated” at the metal-rich end via predictions of photoionization models (e.g., Edmunds & Pagel 1984, Kewley & Dopita 2002). Unfortunately, models for metal-rich nebulae are rather sensitive to details of input parameters (stellar fluxes, density, dust), and so various strong-line calibrations have differed by factors of 2-3 or more, provoking considerable debate. Thus, direct temperature measurements would be a valuable resource for understanding the strong-line - O/H relationship.

The Local Group galaxy M33 is an excellent candidate for studying gas phase element abundances in the interstellar medium (ISM). Because of its proximity to our own galaxy, wealth of H II regions (Boulesteix et al. 1974; Courtès et al. 1987), and relatively low inclination, it has been the subject of much study over the past 65 years. Aller (1942) obtained the first spectroscopy of H II regions in M33 and found a radial gradient in the strength of [O II] and [O III] emission lines across the galaxy, and suggested that it could be due to a gradient in excitation. Smith (1975) was among the first to successfully measure [O III] λ 4363 and thus to derive electron temperatures for H II regions in several spiral galaxies, including M33. This supported the hypothesis of Searle (1971) that a composition gradient, not a gradient in the excitation, was responsible for the radial variation of oxygen forbidden line strengths.

Since then several more studies have been carried out concentrating on determining a comprehensive abundance distribution for M33. Kwitter & Aller (1981) used the [O III] $\lambda\lambda$ 4959, 5007/ λ 4363 and [O II] λ 3727/ λ 7325 line ratios to compute electron temperatures for seven H II regions. They derived an oxygen gradient of -0.13 dex/kpc and noted that Ne, N, S, and Ar followed essentially the same gradient. Vílchez et al. (1988) combined IPCS and CCD observations and derived electron temperatures for [O II], [O III], and [S III] for five giant H II regions. They derived a similar oxygen gradient of -0.12 dex/kpc. Garnett et al. (1997) compiled data collected by the above studies and recalculated abundances using updated atomic coefficients, and obtained an oxygen abundance gradient of -0.11 ± 0.02 dex/kpc for M33.

Oxygen and neon are both produced mainly in stars larger than 10 solar masses, which have very short lifetimes. From stellar nucleosynthesis calculations (e.g., Woosley & Weaver 1995), it is expected that the abundances of neon and oxygen should trace one another closely; the chemical evolution calculations of Timmes, Woosley, & Weaver (1995), predict that the O/Ne ratio varies by no more than 0.1 dex over the range $-1.5 < [\text{Fe}/\text{H}] < 0.0$ (which corresponds roughly to O/H in the range 0.1 to 1.0 times the solar value). This prediction is supported by measurements of abundances in planetary nebulae (Henry 1990), which show that Ne/O is constant over a wide range of O/H.

However, Willner & Nelson-Patel (2002) derived neon abundances for 25 H II regions in M33 from infrared spectroscopy of [Ne II] and [Ne III] fine structure lines using the *Infrared Space Observatory (ISO)*, and reported a Ne/H gradient (-0.034 ± 0.015 dex/kpc) that is significantly shallower than the O/H gradient obtained from the visible-light measurements. The implication is that either set of measurements is in error, or that the Ne/O ratio across M33 varies by 0.5 dex over a factor ten in O/H. In this paper, we report visible-light CCD spectroscopy of H II regions in M33 to directly measure electron temperatures, and if possible to resolve the discrepancy between the results from infrared and visible-light spectra.

2. Observations and Data Reduction

Spectra of 13 H II regions were obtained on September 27-29, 1992 using the Mayall 4 m telescope at Kitt Peak National Observatory. The data were taken using the R-C CCD spectrograph with a spectral range of 3600-5100 Å at approximately 2 Å resolution with a slit width of 1"8. The long slit of the spectrograph was often oriented so that multiple H II regions could be observed at once. Risley prisms were used to compensate for not being at the parallactic angle. A list of the H II regions observed for this study is given in Table 1. It presents the coordinates for the center of each object, the position angle of the slit in degrees measured from North through East, and the deprojected distance of each H II region from the nucleus. The coordinates were measured from Mosaic H α imaging of M33 obtained by Massey et al. for the Survey of Resolved Stellar Content of Local Group Galaxies¹. We assumed a distance of 832 kpc to M33 (Wilson et al. 1990), an inclination angle of 56° and a position angle of 23° (Zaritsky et al. 1989). The nucleus of M33 was measured to be RA = 1^h 33^m 50.9^s, Dec = +30° 39' 37".2 (J2000) from the Mosaic H α image.

The data reduction followed standard procedures. We divided a normalized two-dimensional flat field, constructed using a combination of quartz lamp exposures to derive the pixel-to-pixel sensitivity variations plus a twilight sky exposure to correct for vignetting, into each spectrum. Comparison of the normalized flat field frames taken at different times during the run showed that the flat fields were reproducible to a level of about 0.6% r.m.s. The spectra were rectified and placed on a wavelength scale using exposures of a He-Ne-Ar lamp; a cubic fit to the dispersion data gave residuals of approximately 0.2 Å r.m.s. Flux calibration of the spectra was performed using observations of the spectrophotometric standard stars Wolf 1346, BD+28 4200, Feige 110, G191B2B, Hiltner 600, and Feige 34, all of which were observed at least once during the course of each night. We derived the instrument sensitivity function by fitting a low-order spline fit to the standard star measurements. We corrected all of the standards and object spectra for atmospheric extinction using mean KPNO extinction coefficients. Since the data were taken through a narrow slit, absolute spectrophotometry was not possible, and we averaged the various standard star sensitivity measurements at each wavelength to derive the sensitivity function. Based on the residuals of the data from the fit, the relative calibration across the spectrum is good to about 2.5% .

Emission line strengths were measured using the SPLIT task in IRAF's ONEDSPEC package. The emission lines were fit with Gaussian profiles and integrated in order to obtain a measurement of the flux. A linear background was also fit and subtracted from the profile. In the instance when two lines overlapped but were still resolved (e.g. the [O III] λ 4959 and λ 5007 lines), the line strengths were deblended by fitting the profiles concurrently with the constraint that both lines be fit with the same FWHM.

Interstellar reddening toward each H II region was determined by comparing observed hy-

¹<http://archive.noao.edu/nsa/massey.html>

drogen Balmer emission line ratios to the theoretical Balmer decrement of Hummer and Storey (1987). The average interstellar extinction curve, $f(\lambda) - f(H\beta)$, was taken from Savage and Mathis (1979). We corrected the Balmer line strengths for underlying photospheric absorption by incrementing the equivalent width of stellar absorption in 0.1 Å intervals from 0.1 Å to 3.0 Å. For each value of the equivalent width, we determined the logarithmic reddening coefficient, $c(H\beta)$, for the $I(H\gamma)/I(H\beta)$, $I(H\delta)/I(H\beta)$, and $I(H9)/I(H\beta)$ line ratios, giving us three independent estimates for $c(H\beta)$. The adopted value for the equivalent width of underlying absorption was chosen such that the dispersion in $c(H\beta)$ for each object was minimized. The weighted mean of the three logarithmic reddening coefficients was then computed and used to correct the line strengths for interstellar reddening. The error in the weighted mean was taken as the uncertainty.

The dereddened emission line strengths for each object are listed in Tables 2 and 3. The adopted logarithmic reddening coefficient and the equivalent width of underlying photospheric absorption are also listed for each object. The method by which we computed the uncertainties in the dereddened line strengths and the logarithmic reddening coefficients is described in Section 3.3.

3. Emission Line Analysis

Electron temperatures, densities, and ionic abundances were computed using the N-level atom code found in IRAF’s NEBULAR package, a detailed description of which can be found in Shaw & Dufour (1995). This code is based upon the five-level atom code of De Robertis, Dufour, & Hunt (1987), but is more robust in that it allows for more than five levels for most ions.

3.1. Electron Temperatures and Densities

Table 4 lists the derived measurements or upper limits for electron density, n_e , estimated from the [O II] $\lambda 3726/\lambda 3729$ line ratio. All n_e calculations were performed using the IRAF task TEMDEN, assuming an electron temperature of 10,000 K. All but one of the observed H II regions (BCLMP691) had an [O II] line ratio with a 1σ uncertainty which included the theoretical low density limit. As a result, we computed 2σ upper limits for n_e for all sources but BCLMP691 based on the formal uncertainties in the dereddened [O II] line ratios. The derived estimates and upper limits for n_e place all of the H II regions in the low density regime ($n_e \lesssim 300\text{cm}^{-3}$).

The commonly used [O III] $\lambda\lambda 4959, 5007/\lambda 4363$ line ratio was the only diagnostic available for deriving the electron temperature. Of the 13 spectra collected, six contained a detectable [O III] $\lambda 4363$ line. We were thus able to compute electron temperatures for just under half of the H II regions observed. Electron temperatures were computed by again using the IRAF task TEMDEN assuming an electron density of $n_e = 100\text{cm}^{-3}$. Table 4 lists the derived values for T[O III] along with their uncertainties.

3.2. Ion and Element Abundances

We estimated ion abundances for the six H II regions which had a T[O III] measurement. Table 5 lists the ionic abundances which we were able to derive: O^+ , O^{+2} , and Ne^{+2} , along with their uncertainties. All abundance calculations were performed using the IRAF task IONIC. Abundances for O^+ and O^{+2} were computed using the summed line ratios of [O II] $\lambda\lambda 3726, 3729$ and [O III] $\lambda\lambda 4959, 5007$ respectively. Abundances for Ne^{+2} were computed using the [Ne III] $\lambda 3869$ line. All of the regions studied have electron densities too low for collisional de-excitation of the forbidden lines to be important.

We assumed a two-zone model for the electron temperature structure for the abundance calculations. From ionization models, Garnett (1992) found that the temperatures in the Ne^{+2} and O^{+2} zones were essentially equal; therefore, we used T[O III] to compute abundances for O^{+2} and Ne^{+2} , while for O^+ we used estimates for T[O II] based on the relation between T(O^+) and T(O^{+2}) from Campbell et al. (1986) and Garnett (1992),

$$t(O^+) = 0.7t(O^{+2}) + 0.3, \quad (1)$$

where $t = T_e/10^4 K$. (In this format, temperatures specified by the ionic species, e.g. T(O^{+2}), refer to the ion-weighted average temperature for that species, while temperatures specified by spectroscopic notation, e.g. T[O III], refer to temperatures computed directly from the spectra.)

Table 5 also lists the total element abundances for neon and oxygen along with their uncertainties. We assumed that all of the oxygen and neon was either in the singly or doubly ionized state, except in the case of the two newly identified He II emitting regions. For those objects, we assumed that $O^{+3}/O \approx He^{+2}/He$, based on the similarity in their ionization potentials. This should be an accurate approximation when the He^{+2} fraction is small, and we indeed find that only a very small fraction (3% for BCLMP090 and 6% for MA1) of oxygen is triply ionized in these regions. The ionization fraction for Ne^{+3} is even smaller because of its larger ionization potential.

If we assume that the emission is optically thin, the total element abundance is equal to the sum of the singly and doubly ionized components. This computation is easily carried out for oxygen. Neon, however, presents a problem because [Ne II] is not seen in the visible spectrum. Total element abundances for neon were therefore estimated by computing an ionization correction using photoionization models from Stasińska, Schaerer, & Leitherer (2001). For the purposes of this study we did use a subset of their model grid: we used the instantaneous burst models with Salpeter IMF and upper stellar mass limit 120 solar masses (model sequences IKF, IKI, and IKL). These model sequences were further restricted to those with refractory elements depleted onto grains (depletion = 0.1 times the normal values). Figure 1 is a plot of $X(Ne^{+2})/X(O^{+2})$ vs. $X(O^{+2})$ as predicted by the photoionization models, where $X(O^{+2}) = O^{+2}/(O^+ + O^{+2})$ and $X(Ne^{+2}) = Ne^{+2}/(Ne^+ + Ne^{+2})$. According to the models, for $X(O^{+2}) \gtrsim 0.05$, the ratio

$X(Ne^{+2})/X(O^{+2})$ is approximately one. Therefore, we assume

$$\frac{Ne}{H} = \left(\frac{O^+ + O^{+2}}{O^{+2}} \right) \frac{Ne^{+2}}{H^+}. \quad (2)$$

To add additional points and better constrain the neon and oxygen abundance gradients, we included several H II regions having electron temperature measurements from Vílchez et al. (1988). To be consistent in the atomic data used, we re-computed electron temperatures and abundances for the Vílchez et al. (1988) objects in the same way as for our new sample. For all but two of the Vílchez sources, there was an [O III] $\lambda\lambda 4959, 5007/\lambda 4363$ line ratio available for computing T[O III]. For the two sources, NGC595 and MA2, where T[O III] could not be measured, the [S III] $\lambda\lambda 9069, 9532/\lambda 6312$ and [O II] $\lambda 3727/\lambda 7325$ line ratios were employed respectively to derive electron temperatures. For MA2, we used the calibration,

$$T(S^{+2}) = 0.83T(O^{+2}) + 1700K \quad (3)$$

derived in Garnett (1992) to estimate $T(O^{+2})$. Table 6 lists the measured electron temperature along with the deprojected distance from the nucleus of each H II region in the Vílchez study from which an electron temperature could be measured. Table 7 lists the ion and element abundances for those sources.

3.3. Uncertainties

Uncertainties in the line fluxes, σ_{line} , were computed by adding in quadrature the statistical uncertainty introduced by the photon noise, $\sigma_{stat.}$, the uncertainty in the flat fielding correction, σ_{ff} , and the uncertainty in the photometric calibration, σ_{phot} ,

$$\sigma_{line} = \sqrt{\sigma_{stat}^2 + \sigma_{ff}^2 + \sigma_{phot}^2}. \quad (4)$$

The statistical uncertainty was estimated from the noise in the continuum using the formula (Pérez-Montero & Díaz 2003),

$$\sigma_{stat} = \sigma_{cont} N^{1/2} \left(1 + \frac{EW}{N\delta\lambda} \right)^{1/2} \quad (5)$$

where σ_{cont} is the r.m.s. dispersion in the continuum, N is the number of pixels in the window over which the line was measured, EW is the equivalent width of the line in \AA , and $\delta\lambda$ is the dispersion in $\text{\AA}/\text{pixel}$. The first term in the sum represents the contribution of the continuum noise to the total statistical uncertainty, while the second term represents the contribution of the photon noise from the line itself. The r.m.s. uncertainty in the flat field was approximately 0.6%, determined by comparing flat field exposures taken at different times during the run. The relative end-to-end uncertainty in the flux calibration across the spectrum was approximately 2.5%.

The error in $c(H\beta)$ was computed by formally propagating the uncertainty from the line strengths, $I(\lambda)$,

$$\sigma_{c(H\beta)} = \sigma_{I_\lambda/I_{H\beta}} \left[\frac{1}{\ln(10)[f(\lambda) - f(H\beta)](I_\lambda/I_{H\beta})} \right] \quad (6)$$

Once the errors in the interstellar reddening coefficients were computed, the uncertainties in the dereddened line ratios, $I_{\lambda_o}/I_{H\beta_o}$, could be determined by again formally propagating the uncertainties,

$$\sigma_{I_{\lambda_o}/I_{H\beta_o}} = 10^{c(f(\lambda)-f(H\beta))} \sqrt{\sigma_{I_\lambda/I_{H\beta}}^2 + \sigma_c^2(I_\lambda/I_{H\beta})^2(f(\lambda) - f(H\beta))^2 \ln(10)^2}. \quad (7)$$

We estimated the uncertainty in the electron temperature using a Monte Carlo simulation. Assuming that the error in the [O III] $\lambda\lambda 4959, 5007/\lambda 4363$ line ratio can be accurately characterized by a Gaussian profile, a measured line ratio and the error in that ratio can be interpreted respectively as the mean and standard deviation of a Gaussian distribution. This distribution can then be populated by means of a Monte Carlo simulation which generates deviates drawn from a Gaussian distribution. The method used to compute the deviates is described in section 5.4 of Bevington & Robinson (2003).

We populated each distribution with 10,000 deviates and fed them into the N-level atom code to produce a corresponding distribution of electron temperatures. Because of the logarithmic dependence of T_e on its diagnostic line ratio, the temperature distributions were asymmetric and skewed such that the expectation value for a distribution was offset from the value computed directly from the line ratio. The line ratios with the largest uncertainties yielded the most highly skewed and biased temperature distributions. For BCLMP706 this offset was most prominent (~ -500 K); BCLMP745 and MA2 also had large offsets (~ -400 K). The rest of the H II regions had small temperature offsets (< 200 K). We therefore chose to determine the expectation values for the temperature distributions from the histogram of each distribution. Note that in the case of the largest T_e difference (BCLMP706), the change in O/H is less than 0.1 dex.

Because the temperature distributions were asymmetric, using a single Gaussian to characterize the uncertainty in an electron temperature measurement was not appropriate. We therefore used the expectation value to divide the distribution into two sections. Deviates less than the expectation value were used to characterize the negative error and deviates greater than the expectation value were used to characterize the positive error. We assumed that the profile in each case could be modeled by one-half of a Gaussian profile, and used a fit to determine the one-sided standard deviation for the distribution on either side of the expectation value. The two values for the standard deviation thus derived were taken to be the negative and positive uncertainties for T_e .

The uncertainty in the ionic abundances were computed using the same technique. The total error in these measurements, however, came from two sources: the error in the emission line flux (which we assume is normally distributed) and the error in the electron temperature (which has a skewed distribution as described above). We therefore modeled the abundance errors with a Monte

Carlo analysis, feeding in both sources of error. The resulting uncertainties are those listed in Tables 5 and 7.

4. Two New He II-emitting H II Regions in M33

We report here the discovery of two new examples of H II regions that emit nebular He II $\lambda 4686$ emission in M33. Nebular He II emission is a phenomenon seen in only a handful of H II regions in Local Group galaxies (Garnett et al. 1991). No single cause has been identified for the source of the He II emission in such objects; He II emission has been observed in nebulae associated with WO and peculiar WN stars, high-mass X-ray binaries, and in one case with an otherwise ordinary mid-O type main sequence star (Pakull & Angebault 1986; Stasińska et al. 1986; Garnett et al. 1991; Garnett et al. 2000). To date, these He II nebulae have been found primarily in metal-poor dwarf irregular galaxies, except for the Galactic Wolf-Rayet bubble G2.4+1.4 associated with the WO star WR 102 (Dopita et al. 1990). Narrow He II emission has also been found in a number of metal-poor dwarf starburst galaxies, as catalogued in Schaerer, Contini, & Pindao (1999). The two objects discovered in this study are the first He II nebulae identified in a spiral galaxy beyond the Milky Way.

The first new He II region in M33 is BCLMP090, a small, relatively faint H II region about 1 kpc from the center of the galaxy. BCLMP090 has a diameter of roughly $7''$ as measured from the $H\alpha$ image from the MOSAIC Survey of Local Group Galaxies. The nebular morphology consists of a knot on the northwest side, opening out into a ring toward the southeast. Its diameter of about 30 pc clearly shows that this is not a planetary nebula. Figure 2 shows a portion of our spectrum of BCLMP090. The plot shows the detections of He II $\lambda 4686$ and [O III] $\lambda 4363$; [Ar IV] $\lambda 4740$ may also be detected marginally, which would be consistent with the presence of He II emission. The high [O III] $\lambda 5007/H\beta$ ratio of 6.6 (see Table 2) is very uncharacteristic of H II regions with similar O/H, providing further support for the high excitation and ionization state of BCLMP090.

Because of the narrow spectrograph slit used, we are not able to measure total $\lambda 4686$ and $H\beta$ fluxes very accurately. The fluxes measured within the slit, corrected for reddening, are $F(\lambda 4686) = 3.1 \times 10^{-16} \text{ erg cm}^{-2} \text{ s}^{-1}$ and $F(H\beta) = 1.1 \times 10^{-14} \text{ erg cm}^{-2} \text{ s}^{-1}$. Examination of the spatial profile across the slit showed that the He II emission covered a region about $2''.8$ across (FWHM). With a $1''.8$ slit, this indicates that the total $\lambda 4686$ flux is probably no more than two times larger than the measured flux within the slit. $H\beta$ is emitted over a much larger area, and we crudely estimate that the total $F(H\beta)$ is 3-4 times larger than the value measured within the slit. Assuming a distance of 832 kpc to M33, we thus estimate $L(\lambda 4686) \approx 5 \times 10^{34} \text{ erg s}^{-1}$ and $L(H\beta) \approx 3 \times 10^{36} \text{ erg s}^{-1}$. These values are slightly lower than, but consistent with, those measured for other He II nebulae, while the $L(\lambda 4686)/L(H\beta)$ ratio is entirely consistent with those for other objects (Garnett et al. 1991).

The observed continuum in BCLMP090 is faint and shows no obvious stellar features other than Balmer absorption lines, so we are not able to provide a classification for the star, except that

it does not appear to be a Wolf-Rayet star. The measured $L(\text{H}\beta)$ is consistent with that of a late O-type main sequence star. We searched the catalogs of X-ray sources in M33 derived by Pietsch et al. (2004) from *XMM-Newton* observations, and from *Chandra* observations by Grimm et al. (2005). We found no source within one arcmin of the position of BCLMP090 with $L_X > 2 \times 10^{34}$ erg s^{-1} . This indicates that BCLMP090 is not an X-ray ionized nebula powered by a currently-active X-ray binary, as exemplified by LMC-N159F, which is powered by the massive binary LMC X-1 (Pakull & Angebault 1986).

The second He II nebula we identified is MA 1, the outermost known H II region in M33. MA 1 was observed previously by McCall, Rybski, & Shields (1985) and Garnett, Odewahn, & Skillman (1992), who demonstrated the low O/H of the nebula. MA 1 is a large H II complex approximately $45''$ in diameter, consisting of a bright knot surrounded by extensive nebular filaments. Garnett et al. (1992) noted the presence of He II $\lambda 4686$ emission in MA 1, but they were not able to determine definitively whether the emission was nebular or stellar.

With our new high signal/noise spectrum of MA 1, we are able to confirm that the narrow He II emission is spatially extended, and thus is nebular in nature. Figure 3 shows spectra from two positions in MA 1. The first position corresponds to the bright knot and includes the stellar object “star 1” noted by Garnett et al. (1992), which is probably a star cluster. At this position the spectrum shows the nebular He II emission plus a strong stellar continuum with a number of absorption features (e.g., He II $\lambda 4512$, Si IV $\lambda\lambda 4089, 4116$, He I $\lambda\lambda 4120, 4143, 4387, 4471$) characteristic of OB stars. The second spectrum, from a position $9''$ E of the first shows no nebular He II emission, but rather the broad He II feature characteristic of a WN star, one of two spectroscopically confirmed WN stars (MC 8 and MC 9) in MA 1 (Massey & Conti 1983).

Meanwhile, Figure 4(a) shows the spatial profile of both the $\lambda 4686$ emission and the stellar continuum, while Figure 4(b) shows the spatial profile of the He II emission with the stellar continuum subtracted – that is, only pure nebular He II emission or the W-R $\lambda 4686$ feature. The regions of nebular He II emission and the position of the WN star are marked. It is notable from Figures 3 and 4 that the nebular He II emission is not strongest at the position of the W-R star, but rather at the position of the OB cluster, more than 30 pc away. While it is not possible to completely rule out that the W-R star is powering the He II emission, the poor spatial correlation argues strongly against the W-R star being the source of He^+ -ionizing photons. We conclude that the He II nebula is powered by a source(s) within the OB star cluster. This distinction is significant, as narrow (presumed nebular) He II emission is often associated with the presence of Wolf-Rayet stars (e.g., Izotov et al. 1997), and it is often argued that this demonstrates that Wolf-Rayet stars are responsible for the nebular emission. Our new observations of MA 1 provide evidence that it is not safe to automatically associate nebular He II emission with Wolf-Rayet stars based on an integrated spectrum.

As we did for BCLMP090, we estimate roughly the He II and $\text{H}\beta$ fluxes for MA 1, keeping in mind that this estimate is more uncertain because the spectrograph slit subtends a much smaller

fraction of MA 1. We measured $F(\lambda 4686) = 1.2 \times 10^{-15} \text{ erg cm}^{-2} \text{ s}^{-1}$ over a region about $8''$ across. If we assume uniform surface brightness over a circular region with diameter $8''$, we derive $L(\lambda 4686) \approx 5 \times 10^{35} \text{ erg s}^{-1}$. This value may be accurate to no more than a factor of two; nevertheless, the derived flux is still similar to the values derived by Garnett et al. (1991) for other He II nebulae. A more precise value would require a measurement of the He II flux over the entire emission region. Such measurements are desirable to accurately determine the He II luminosities and to constrain the parameters of the ionizing stars.

Given the lack of association between the He II emission in MA 1 and the W-R star, it is not possible at present to identify the likely source powering the He II emission. The *XMM – Newton* observations of M33 show no X-ray point source at the location of MA 1 (Pietsch et al. 2004); the nearest point source is $13''$ north of the region we observed, making an association unlikely. (Grimm et al. 2005 did not observe this field with *Chandra*.) More extensive observations of these objects are desirable to identify the likely ionizing stars, constrain their atmospheric parameters, and ultimately to produce a much clearer picture of how He II emission is produced in these objects and whether or not these peculiar ionizing stars are natural products of stellar evolution.

5. Oxygen and Neon Abundance Gradients

The abundance measurements vs. deprojected galactocentric radius for both O/H (top) and Ne/H (bottom) are displayed in Figure 5. We also show in Figure 5 the data for H II regions with measured electron temperatures from Vílchez et al. (1988). These two data sets give O/H gradient slopes (-0.03 ± 0.01 for our data vs. -0.004 ± 0.03 for the Vílchez et al. points) and zeropoints (-3.62 ± 0.05 vs. -3.55 ± 0.13) that agree to within 1σ ; similarly, we find agreement to within 1.3σ for the Ne/H gradients. Therefore, although there appears to be a slight systematic offset between the two data sets, the offset is statistically insignificant, and we combine the two sets of points to estimate the O/H and Ne/H gradients for this and all subsequent discussion in this paper. The dashed lines in Figure 5 represent the resulting O and Ne abundance gradients based on a weighted linear least squares fit to the combined data from this study and the five points from Vílchez et al. (1988). The least squares fit for the O/H gradient is $-0.012 \pm 0.011 \text{ dex/kpc}$ and the least squares fit for the Ne/H gradient is $-0.016 \pm 0.017 \text{ dex/kpc}$. The newly-derived O/H and Ne/H gradients are in good agreement with each other (within 1σ).

Willner & Nelson-Patel (2002) used the [Ne II] $12.81 \mu\text{m}$ and [Ne III] $15.56 \mu\text{m}$ fine structure lines with radio continuum measurements to measure Ne abundances in M33. These measurements have the advantage of being almost completely temperature independent because both the fine structure lines and the thermal continuum have similar temperature dependences. From their sample of 25 H II regions Willner & Nelson-Patel (2002) derived a Ne/H gradient of $-0.034 \pm 0.015 \text{ dex/kpc}$. Our new measurement of the Ne and O gradients are now only slightly more than 1σ from the Willner & Nelson-Patel (2002) results.

Our new oxygen gradient is much shallower than previous studies have indicated. Garnett et al. (1997) recompiled data from several studies in the literature (Smith 1975; Kwitter & Aller 1981; Vílchez et al. 1988; Garnett, Odewahn, & Skillman 1992) which measured oxygen abundances in H II regions. They computed an oxygen gradient of -0.11 ± 0.02 dex/kpc for M33. We note that many of the H II regions in these studies did not have measured electron temperatures, necessitating the use of a calibration of the strong [O II] and [O III] lines vs. O/H to estimate abundances (Edmunds & Pagel 1984). Several recent studies (Castellanos et al. 2002; Kennicutt, Bresolin, & Garnett 2003; Bresolin, Garnett, & Kennicutt 2004) have now derived T_e , from measurements of [N II] and [S III] line ratios, in a number of metal-rich H II regions in NGC 1232, M101, and M51. These studies have found H II regions with O/H as high as the solar value or slightly higher. They have also shown that abundances based on directly measured electron temperatures are significantly smaller (0.3-0.5 dex) than those derived from various strong-line O/H calibrations. Our new results for H II regions in M33 are consistent with these other studies, implying that the inner disk in M33 is not as metal-rich as previously thought. We should emphasize, however, that we have measured abundances for only one object within 2 kpc of the nucleus of M33.

In Figure 6 we display both the neon abundances derived in the present study and those derived by Willner & Nelson-Patel (2002). The solid and dashed lines are the weighted least squares fits to the Willner & Nelson-Patel data and our data, respectively. The two fits show an offset in Ne/H, such that the Willner & Nelson-Patel data are approximately 0.2 dex higher than the results from the visible spectra; this difference is significant at more than the 3σ level. If we remove BCLMP745, the H II region with the lowest neon abundance level, this result is largely unaffected because of the relatively large uncertainty associated with this measurement. We disregard the difference in slope of the neon gradients because of the large error in the value of the slope.

What could be the source of this difference? One possibility that we considered was that the ionization corrections that we used to derive the neon abundances were inaccurate, as they were estimated from photoionization models; the fractional ionization of Ne^{+2} is very sensitive to the stellar radiation field beyond 40 eV, which is still relatively uncertain for O star model atmospheres. If the ionization corrections we used were systematically too small, then we might expect to see an offset in $X(\text{Ne}^{+2})$ between our data set and those measured by Willner & Nelson-Patel (2002), since our H II regions should have similar ionization on average. Figure 7 plots $X(\text{Ne}^{+2})$ as a function of galactocentric radius for our data set and those from Willner & Nelson-Patel (2002). The figure shows that there is no systematic difference in $X(\text{Ne}^{+2})$ between the two studies. The one exception is BCLMP090, which is a He II nebula and thus has a higher Ne ionization than expected for H II regions ionized by normal O and B stars. The results in Figure 7 suggest that ionization corrections are probably not the source of the offset in neon abundance.

Another possibility is that the electron temperature measurements for this study were biased towards higher values, leading to an underestimation of the metallicity. Stasińska (2005) has shown that in photoionization models for high metallicity H II regions ($\log(\text{O}/\text{H}) \gtrsim -3.4$), oxygen abundances based on direct measurements of electron temperatures derived from [O III] line ratios

could lead to biased oxygen abundance estimates. This is brought about by temperature gradients within a nebula that are the result of strong cooling by [O III] and [N III] fine-structure lines. The effect of the bias is that abundances can be underestimated by as much as 0.2 dex when the true O/H is approximately solar ($\log \text{O}/\text{H} = -3.3$). However, this bias is very small at lower O/H, and so would not explain the difference we see between the IR and visible-light measurements at low O/H. A related possibility is that of temperature fluctuations (Peimbert 1967), wherein fluctuations in T_e lead to a derived temperature that is too high (and thus abundances that are too low) compared to the average temperature. Whether temperature fluctuations large enough to affect abundances are present in photoionized nebulae is still a subject of debate (see e.g., Mathis 1995, Liu 2002).

While the discrepancy we see in Ne/H is of concern, we should emphasize that the optical data comprise only a small set, and we still do not have enough data points in the inner disk of M33 to constrain the Ne and O gradients particularly well. A larger data set should settle the nature of the discrepancy. A program is under way to collect new optical spectroscopy from the ground and IR spectroscopy with the *Spitzer Space Telescope* to evaluate the discrepancy we see here.

Figure 8 displays the radial distribution of O/H from all of the H II regions discussed in this paper (*filled squares*), along with O/H measurements from spectroscopy of B supergiants from Monteverde, Herrero, & Lennon (2001; *stars*). Monteverde et al. noted that the supergiant abundances were in reasonable agreement with the results of Vílchez et al. (1988). Nevertheless, from examination of Figure 8 we can say that the radial trend in O/H based on the supergiants is not discordant with what we find, either. This is undoubtedly a result of the relatively large uncertainties in the oxygen abundances. Many more spectroscopic measurements of stars and H II regions in M33 are needed to properly compare the independent results from stellar and gas abundance studies.

A number of important astrophysical relations (such as the Cepheid period-luminosity relation and the I(CO) - N(H₂) relation) have, or may have, a significant dependence on metallicity. The metallicity dependence in many cases is derived using abundances derived from H II regions. Kennicutt, Bresolin, & Garnett (2003) noted that the derived metallicity dependence for such relations would steepen considerably if metallicity gradients in spiral galaxies are flatter than usually supposed, as found in their paper, and in the present work. Here we revisit briefly the correlation between Wolf-Rayet star properties and metallicity.

It has long been known that the relative number of WC-type and WN-type Wolf-Rayet (WR) stars varies with galactrocentric distance within M33, with the center richer in those of type WC (Massey & Conti 1983, Massey & Johnson 1998). This has been taken to be a demonstration of the importance of stellar winds on the evolution of massive stars; stars with higher initial oxygen abundances will have a higher mass-loss rate, and it will hence be easier to produce WC stars (Massey & Johnson 1998). The trend observed within M33 also extends to such low metallicity galaxies such as the SMC, and to the metal-rich galaxy M31 (Massey 2003). A similar trend is seen with metallicity in the relative number of WRs and red supergiants (Massey 2003). Modern

stellar evolutionary theory does a good job of predicting the trend, at least for the relative number of WCs and WNs (Massey 2003, Meynet & Maeder 2005).

Figure 9 shows an updated version of Figure 11 from Massey (2003), showing the relationship between the WC/WN number ratio and the mean O/H. The filled circles represent averages over galaxies or regions within the galaxies; see Massey (2003) and Massey & Johnson (1998) for a complete description of the data for this figure. The oxygen abundances for several galaxies in this plot have been updated with new values from the following sources: LMC and SMC (Garnett 1999); M33 (this work); Milky Way (Deharveng et al. 2000). With the exception of the data point for M31, all of the abundances for the galaxies in Figure 9 have been derived directly from measurements of the electron temperature; the three points for M33 refer to O/H values determined from the least squares fit at 0.8 kpc, 2 kpc, and 5 kpc from the nucleus. The M31 metallicity, in contrast, was derived from the strong [O II] and [O III] emission lines using a relation that is calibrated largely with photoionization models.

We also plot in Figure 9 the recent results for the metallicity dependence of the WC/WN ratio from Meynet & Maeder (2005), who computed the effects of rotation on mixing and stellar evolution. The predicted relationship between WC/WN and O/H is depicted by the region bounded by the dotted line (see also Figure 11 of Meynet & Maeder 2005). The bounds of the region reflect the fact that stars likely exhibit a range of rotation speeds; the upper bound of the region represents main sequence stars rotating at 300 km s^{-1} , while the lower bound represents non-rotating stars. We see that our new abundance values for M33 are still consistent with the predicted correlation (keeping in mind that the WC/WN ratio for the Galaxy is likely to be overestimated because of incompleteness for WN stars – see Massey 2003). While this is reassuring, we note that the M31 data has a much greater impact on the slope of the correlation. The fact that the M31 abundances were derived with a different method raises some concern; as we have noted above, recent measurements of electron temperatures for metal-rich H II regions yield significantly smaller abundances than strong-line calibrations. Furthermore, analyses by Venn et al. (2000) and Smartt et al. (2001) of four supergiants in M31 does suggest an oxygen abundance similar to that of the solar neighborhood, approximately 0.3 dex lower. We have illustrated this by the unfilled circle for M31 in Figure 9, in which case the correlation between WC/WN and O/H would be considerably steeper. Note, however, that the WC/WN ratio for the Milky Way is likely too large due to selection effects (Massey & Johnson 1998). A new, deep spectroscopic study of H II regions (and young massive stars) in M31 would be worthwhile to evaluate this question.

PM and GJ thank Jennifer Hedden for her assistance at the telescope. DRG thanks Katia Cunha for helpful discussions of abundances in blue supergiants, and Steve Willner for discussions of the ISO measurements for M33 H II regions.

REFERENCES

- Aller, L. H. 1942, *ApJ*, 95, 52
- Bevington, P. R., & Robinson, D. K. 2003, *Data Reduction and Error Analysis for the Physical Sciences*(New York, NY: McGraw-Hill)
- Boulesteix, J., Courtès, G., Laval, A., Monnet, G., & Petit, H. 1974, *A&A*, 37, 33
- Bresolin, F., Garnett, D. R., & Kennicutt, R. C., Jr. 2004, *ApJ*, 615, 228
- Campbell, A., Terlevich, R. J., & Melnick, J. 1986, *MNRAS*, 223, 811
- Castellanos, M., Díaz, A. I., & Terlevich, E., *MNRAS*, 337, 540
- Courtès, G., Petit, H., Sivan, J. -P., Dodonov, S., & Petit, M. 1987, *A&A*, 174, 28
- Deharveng, L., Peña, M., Caplan, J., & Costero, R., 2000, *MNRAS*, 311, 329
- De Robertis, M. M., Dufour, R. J., & Hunt, R. W. 1987, *JRASC*, 81, 195
- Díaz, A. I., Terlevich, E., Vílchez, J. M., Pagel, B. E. J., & Edmunds, M. G. 1991, *MNRAS*, 253, 245
- Dopita, M. A., Lozinskaya, T., McGregor, P. J., & Rawlings, S. J., 1990, *ApJ*, 351, 563
- Edmunds, M. G., & Pagel, B. E. J. 1984, *MNRAS*, 211, 507
- Garnett, D. R. 1992, *AJ*, 103, 1330
- Garnett, D. R. 1999, in *IAU Symposium 190, New Views of the Magellanic Clouds*, eds. Y.-H. Chu, N. Suntzeff, J. Hesser, & D. Bohlender, (San Francisco: Astronomical Society of the Pacific), 266
- Garnett, D. R., Galarza, V. C., & Chu, Y.-H., 2000, *ApJ*, 545, 251
- Garnett, D. R., Kennicutt, R. C., Jr., Chu, Y.-H., & Skillman, E. D., 1991, *ApJ*, 373, 458
- Garnett, D. R., Odewahn, S. C., & Skillman, E. D., 1992, *AJ*, 104, 1714
- Garnett, D. R., Shields, G. A., Skillman, E. D., Sagan, S. P., & Dufour, R. J. 1997, *ApJ*, 489, 63
- Henry, R. B. C., 1990, *ApJ*, 356, 229
- Hummer, D. G., & Storey, P. J. 1987, *MNRAS*, 224, 801
- Izotov, Y. I., Foltz, C. B., Green, R. F., Guseva, N. G., & Thuan, T. X., 1997, *ApJ*, 487, L37
- Kennicutt, R. C., Jr., Bresolin, F., & Garnett, D. R. 2003, *ApJ*, 591, 801

- Kewley, L. J., & Dopita, M. A., 2002, *ApJS*, 142, 35
- Kwitter, K. B., & Aller, L. H. 1981, *MNRAS*, 195, 939
- Liu, X.-W., 2002, *RMxAC*, 12, 70
- Massey, P. 2003 *ARAA* 41, 15
- Massey, P., & Conti, P. S., 1983, *ApJ*, 273, 576
- Massey, P. & Johnson, O. 1998, *ApJ*. 505, 793
- Mathis, J. S., 1995, *RMxAC*, 3, 207
- McCall, M. L., Rybski, P. M., & Shields, G. A., 1985, *ApJS*, 57, 1
- Meynet, G., & Maeder, A., 2005, *A&A* 429, 581
- Monteverde, M. I., Herrero, A., & Lennon, D. J., 2000, *ApJ* 545, 813
- Pakull, M. W., & Angebault, L. P., 1986, *Nature*, 322, 511
- Peimbert, M., 1967, *ApJ*, 150, 825
- Pérez-Montero, E., & Díaz, A. I. 2003, *MNRAS*, 346, 105
- Pietsch, W., Misanovic, Z, Haberl, F., Hatzidimitriou, D., Ehle, M., & Trinchieri, G., 2004, *A&A* 426, 11
- Savage, B. D., & Mathis, J. S., 1979, *ARA&A*, 17, 73
- Schaerer, D., Contini, T., & Pindao, M., 1999, *A&AS*, 136, 35
- Searle, L., 1971, *ApJ*, 168, 327
- Shaw, R. A., Dufour, R. J. 1995, *PASP*, 107, 896
- Smartt, S. J., Crowther, P. A., Dufton, P. L., Lennon, D. J., Kudritzki, R. P., Herrero, A., McCarthy, J. K., & Bresolin, F. 2001 *MNRAS*, 325, 257
- Smith, H. E. 1975, *ApJ*, 199, 591
- Stasińska, G. 1982, *A&A*, 48, 299
- Stasińska, G. 2005, *A&A*, 434, 507
- Stasińska, G., Schaerer, D., & Leitherer, C. 2001, *A&A*, 370, 1
- Stasińska, G., Testor, G., & Heydari-Malayeri, M., 1986, *A&A*, 170, L4.

- Timmes, F. X., Woosley, S. E., & Weaver, T. A., 1995, *ApJS*, 98, 617
- Venn, K. A., McCarthy, J. K., Lennon, D. J., Przybilla, N., Kudritzki, R. P., & Lemke, M., 2000, *ApJ*, 541, 610
- Vila-Costas, M. B., & Edmunds, M. G. 1992, *MNRAS*, 259, 121
- Vílchez, J. M., Pagel, B. E. J., Diaz, A. I., Terlevich, E., & Edmunds, M. G. 1988, *MNRAS*, 235, 633
- Willner, S. P., & Nelson-Patel, K. 2002, *ApJ*, 568, 679
- Wilson, C. D., Freedman, W. L., & Madore, B. F. 1990, *AJ*, 99, 149
- Woosley, S. E., & Weaver, T. A., 1995, *ApJS*, 101, 181
- Zaritsky, D., Elston, R., & Hill, J. M. 1989, *AJ*, 97, 97

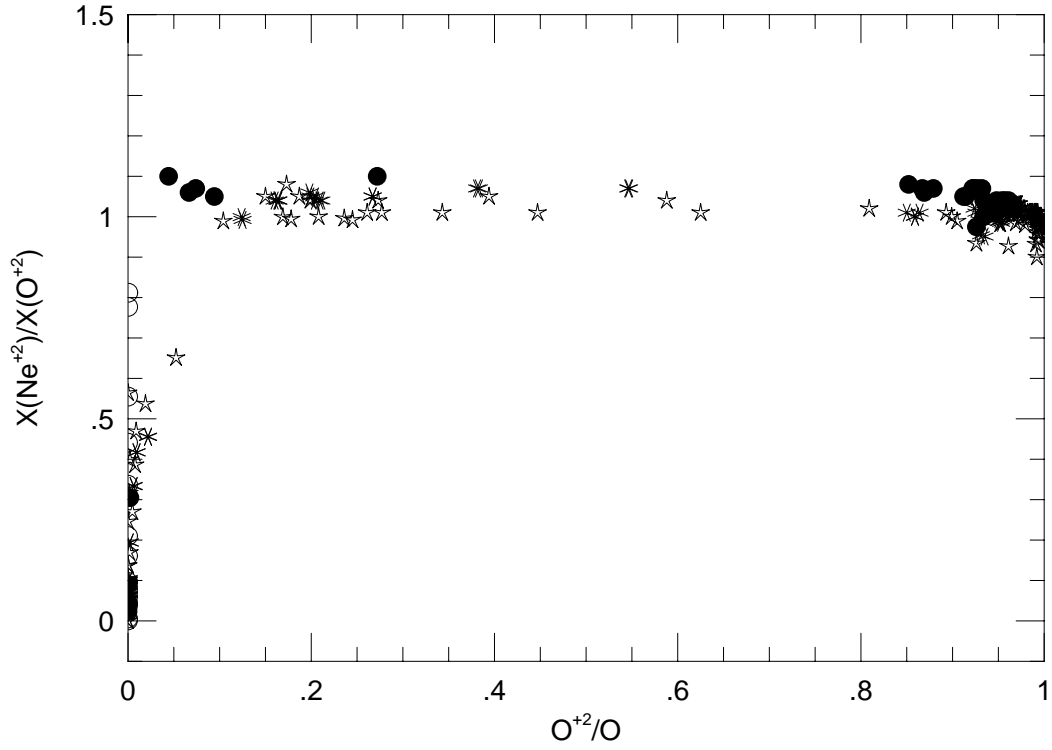


Fig. 1.— The ion ratio $X(Ne^{+2})/X(O^{+2})$ plotted as a function of oxygen ionization, $X(O^{+2})$, as computed by the models of Stasińska, Schaerer, & Leitherer(2001). Filled circles represent the IKF model sequence, asterisks the IKI sequence, and stars the IKL sequence, as discussed in the text. Based on this diagram, when $X(O^{+2}) \gtrsim 0.05$, we can assume that $X(Ne^{+2}) \approx X(O^{+2})$.

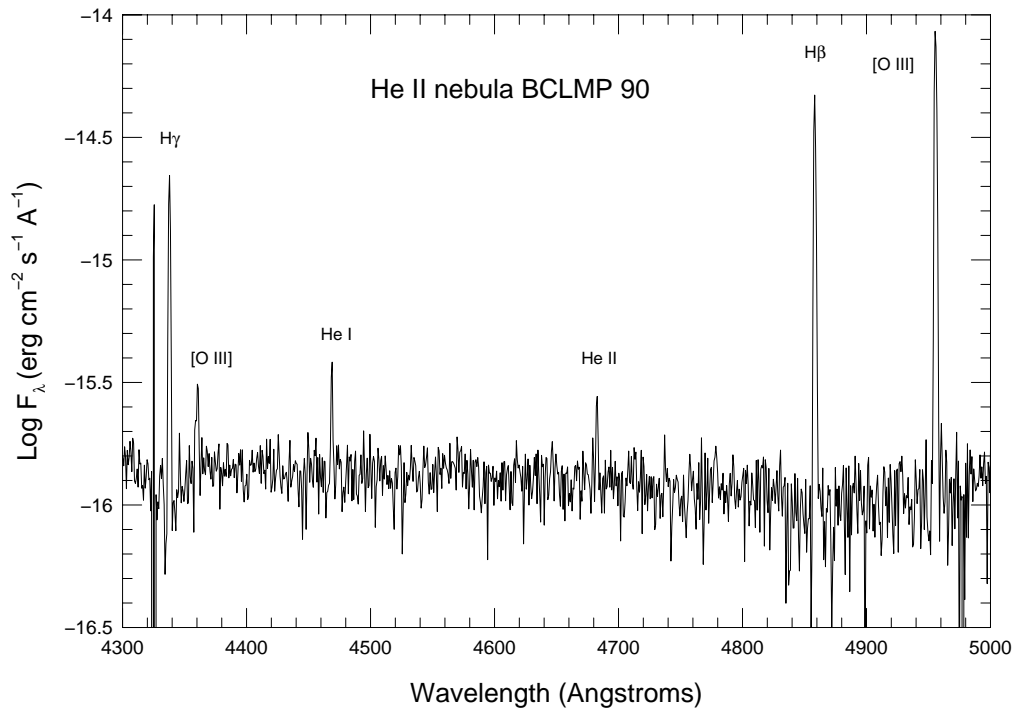


Fig. 2.— A portion of our KPNO 4-m spectrum of the He II nebula BCLMP090 in M33. This segment has been expanded to show our detections of He II λ 4686 and [O III] λ 4363 in this object.

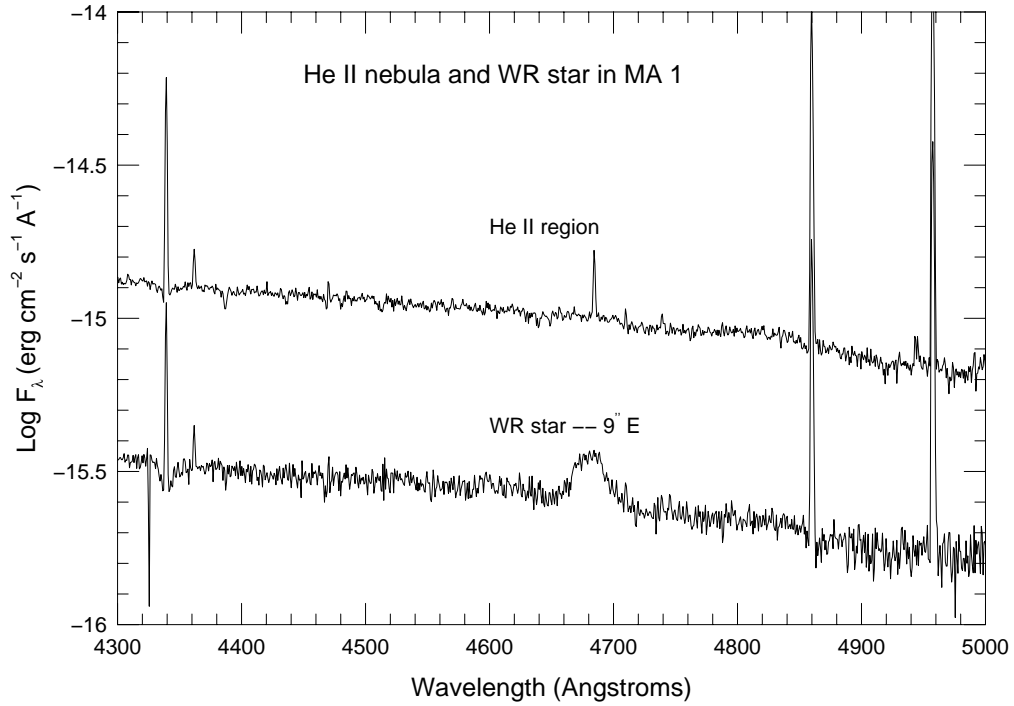


Fig. 3.— A portion of our KPNO 4-m spectrum of the H II region MA 1 in M33. The upper spectrum shows the spectrum of a region within MA 1 that encompasses the He II region and the brighter stellar OB cluster. The lower spectrum shows a part of MA 1 that is $9''$ west of the first position, which includes the WN star discussed in the text. Note the lack of narrow He II $\lambda 4686$ line emission at the position of the WN star.

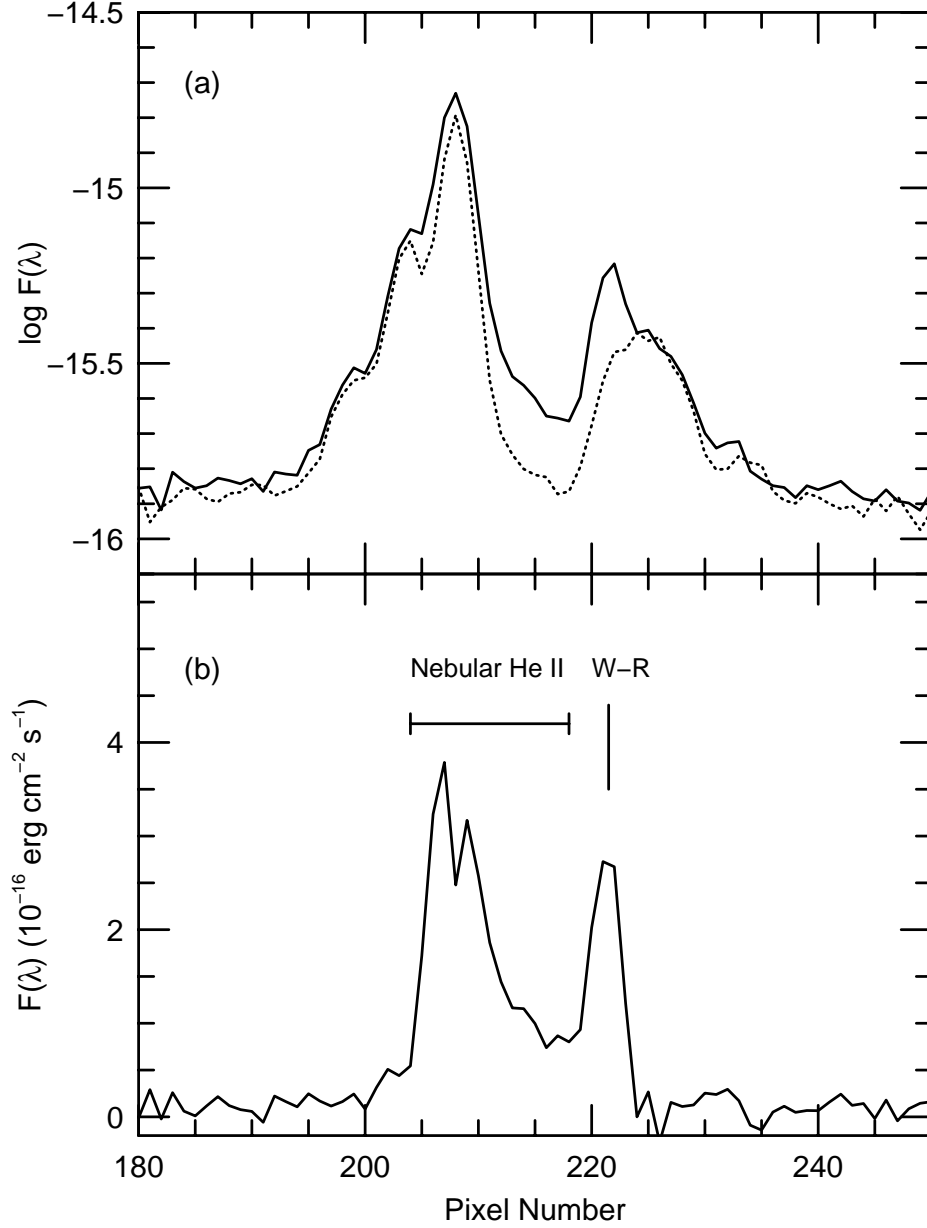


Fig. 4.— (a) A spatial cut of our spectrum of MA 1 along the slit showing the spatial variation of $\lambda 4686$ (*solid line*) and stellar continuum (*dotted line*). (b) The spatial variation of continuum-subtracted He II $\lambda 4686$ emission across MA 1. The locations of the He II nebular emission and the WN star are marked. The scale is $0.72 \text{ arcsec pixel}^{-1}$, and east is to the left in the plots.

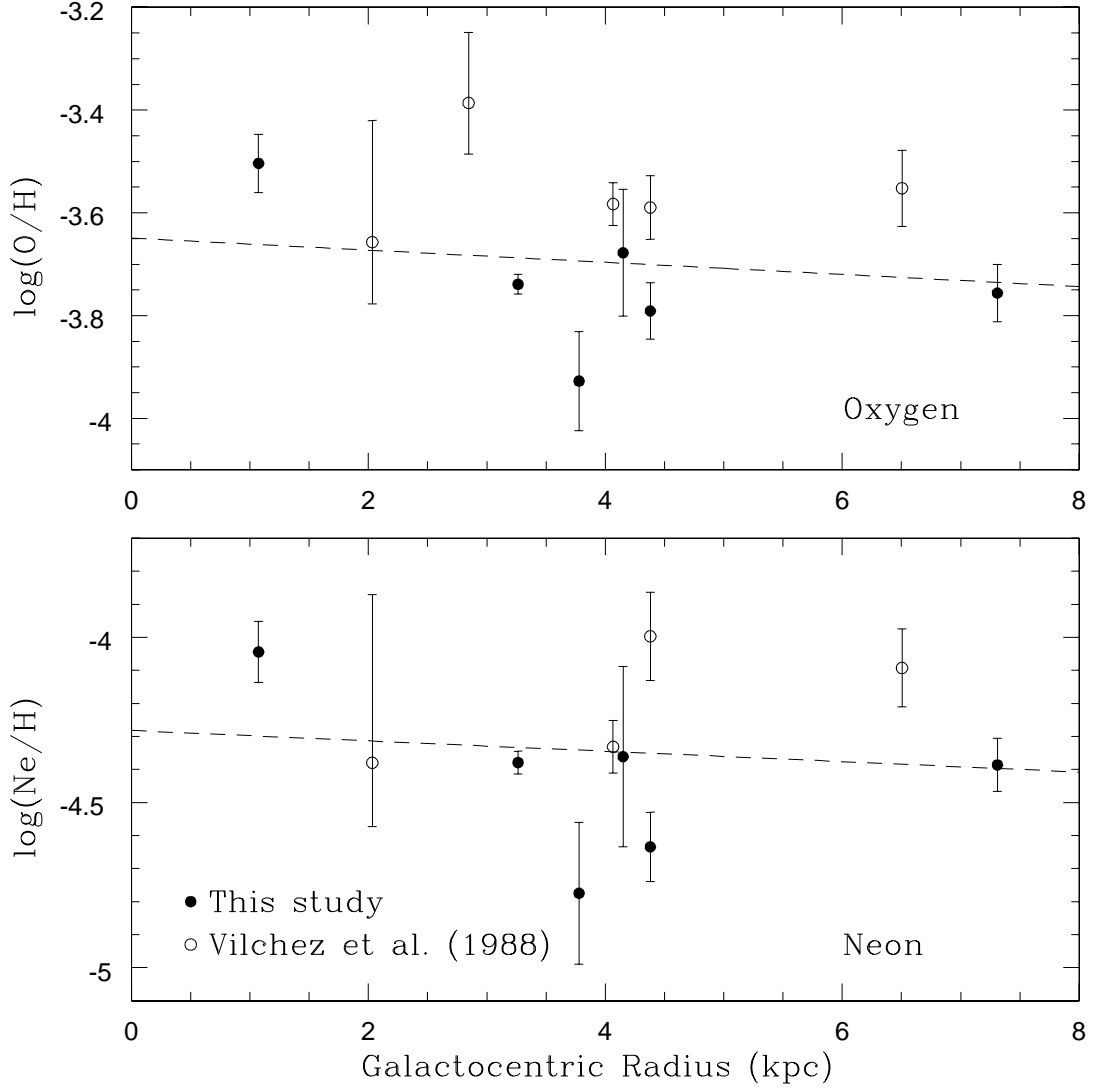


Fig. 5.— $\log(\text{O}/\text{H})$ (top) and $\log(\text{Ne}/\text{H})$ (bottom) plotted as a function of galactocentric radius. Filled circles are abundance measurements from this study and open circles are measurements from Vilchez et al. (1988). The dashed lines in each panel represent the fitted abundance gradients for oxygen and neon based on the combined data from both sets of data plotted.

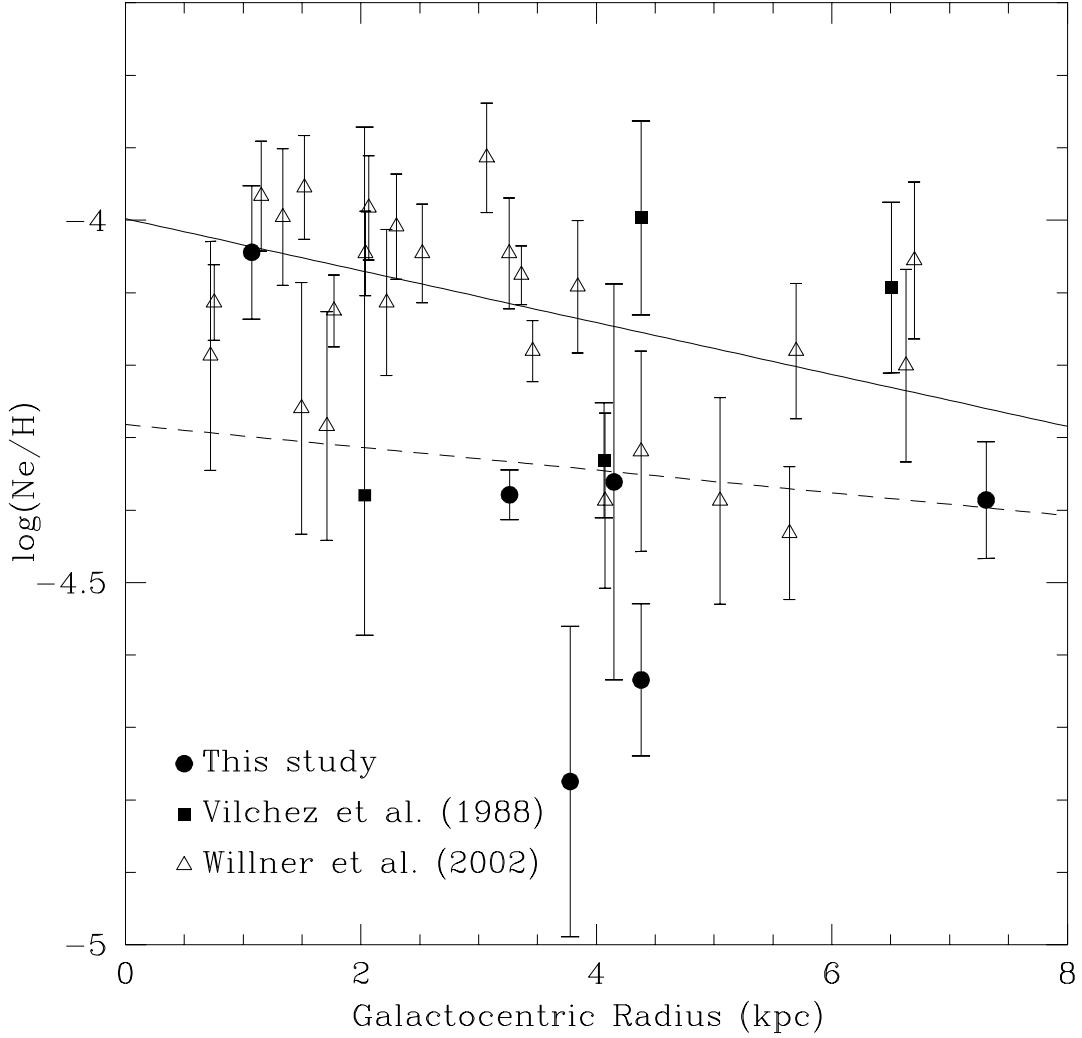


Fig. 6.— Comparison of the overall neon abundances derived by Willner and Nelson-Patel (2002) (triangles) to those derived in this study and Vilchez et al. (1988) (filled circles and filled squares, respectively). The neon gradient derived from the Willner data is shown as a solid line and the gradient derived from this study and the Vilchez data is shown as a dashed line. Note the offset between the two gradients.

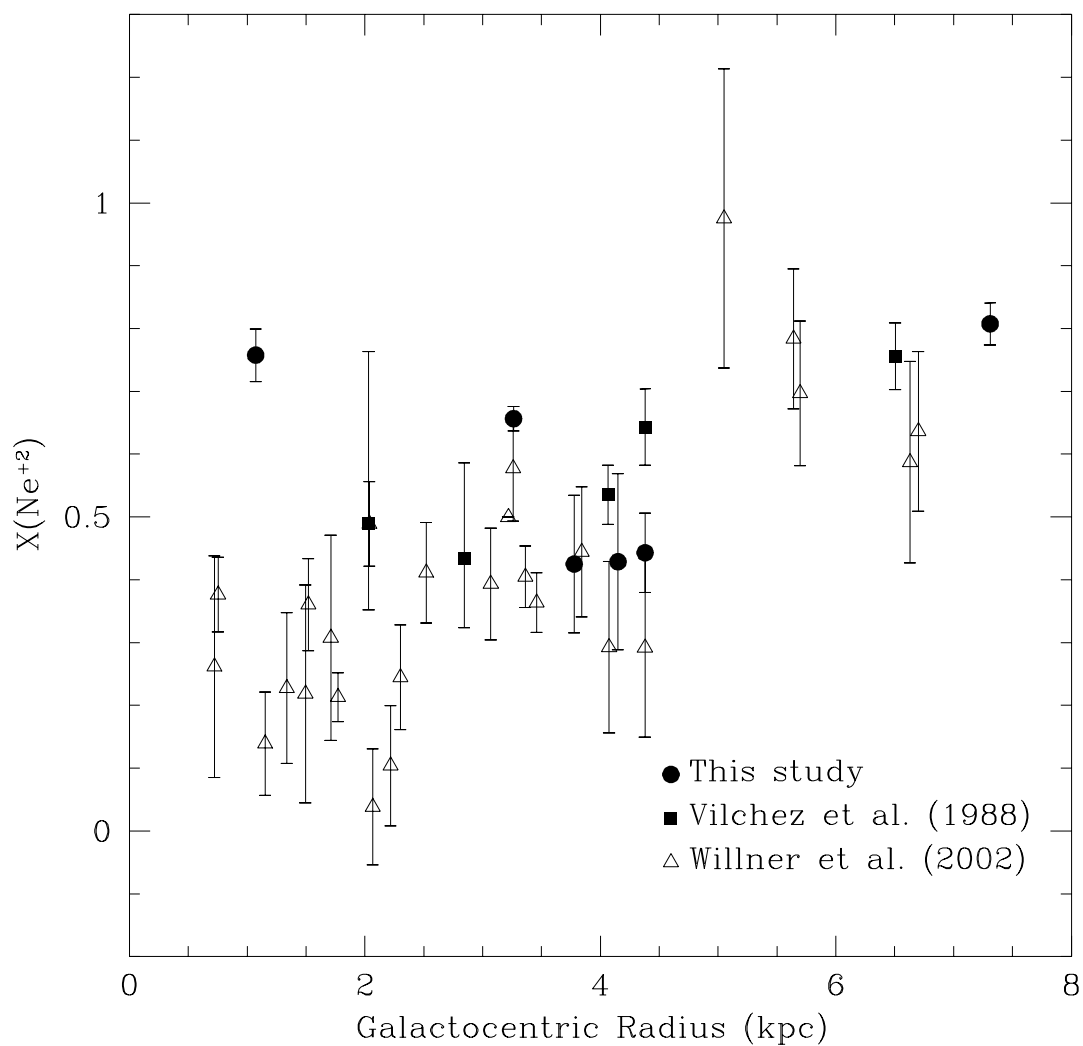


Fig. 7.— Comparison of neon ionization derived from data in this study and Vilchez et al. (1988) to those derived in the Willner study as a function of galactocentric radius. Symbols are the same as in Figure 6. No offset in neon ionization is apparent except for BCLMP094 which is a He II nebula.

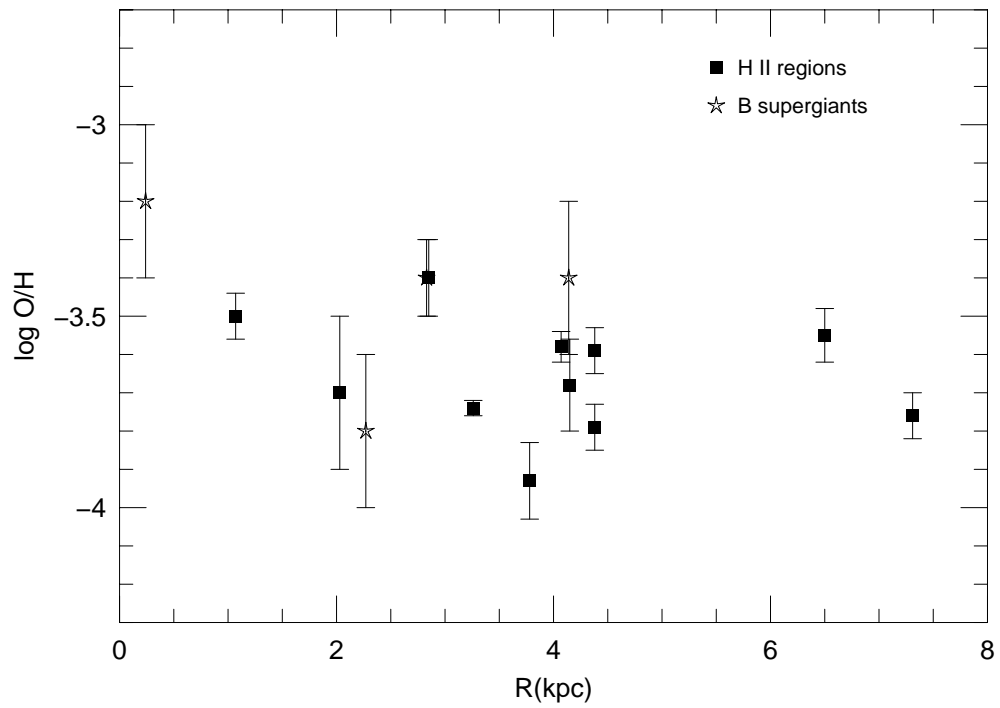


Fig. 8.— Comparison of oxygen abundances in M33 H II regions (*filled squares* – this work) and B supergiants (*stars* – Monteverde et al. 2000).

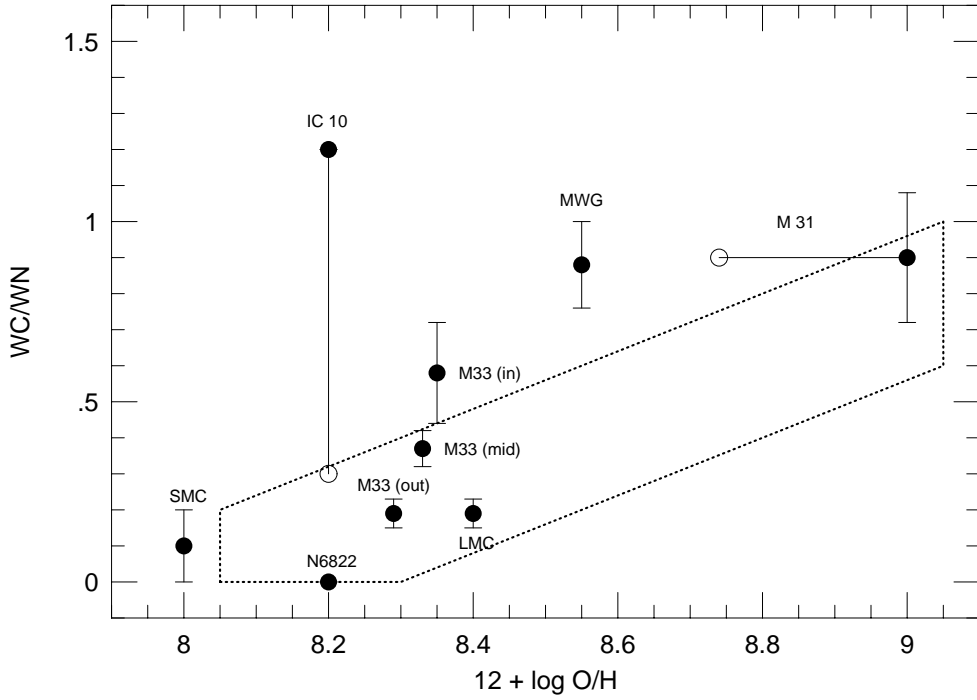


Fig. 9.— The observed correlation between the WC/WN number ratio and oxygen abundance for Local Group galaxies, adapted from Massey (2003). See that paper for a complete discussion of the Wolf-Rayet star data. The points for M33 represent rough average values for O/H at points 0.8 kpc (in), 2 kpc (mid), and 5 kpc (out) from the nucleus. The dotted line shows the range of values predicted by Meynet & Maeder (2005) for rotating and non-rotating stars.

Table 1. H II Region Coordinates And Derived Galactocentric Radii

ID ^a	R.A. (J2000.0)	Decl. (J2000.0)	P.A. deg.	Rad. pc
BCLMP016	1 : 33 : 50.0	30 : 37 : 32.4	53.7	552
BCLMP027	1 : 33 : 45.9	30 : 36 : 50.4	53.7	720
BCLMP094	1 : 34 : 00.4	30 : 38 : 07.6	90.4	769
BCLMP090	1 : 34 : 04.2	30 : 38 : 09.2	90.4	1073
BCLMP696	1 : 33 : 58.4	30 : 48 : 40.1	157.2	2345
CPDSP212	1 : 33 : 57.7	30 : 49 : 02.2	157.2	2456
BCLMP691	1 : 34 : 16.6	30 : 51 : 54.0	90.0	3263
BCLMP745	1 : 34 : 37.6	30 : 34 : 55.0	78.1	3778
BCLMP705	1 : 34 : 40.3	30 : 31 : 20.5	53.3	4017
BCLMP740	1 : 34 : 39.5	30 : 41 : 47.9	90.4	4071
BCLMP706	1 : 34 : 42.2	30 : 31 : 42.3	53.3	4150
BCLMP290A	1 : 33 : 11.4	30 : 45 : 15.1	112.0	4380
MA1 ^b	1 : 33 : 03.4	30 : 11 : 18.7	140.4	7310

^aA BCLMP label denotes an ID from Boulesteix et al. 1974. A CPDSP denotes a label from Courtès et al. 1987, an extension of the Boulesteix study.

^bMA1 does not have a BCLMP or CPDSP ID because it is positioned too far South for both surveys.

Table 2. Dereddened Line Fluxes with Uncertainties

Wavelength	BCLMP016	BCLMP027	BCLMP094	BCLMP090	BCLMP696	CPDSP212	BCLMP691
3725 [O II]	0.83 ± 0.08	1.11 ± 0.08	0.62 ± 0.06	0.80 ± 0.10	1.12 ± 0.10	1.15 ± 0.11	0.73 ± 0.04
3727 [O II]	1.23 ± 0.10	1.59 ± 0.11	0.89 ± 0.07	1.18 ± 0.13	1.67 ± 0.13	1.73 ± 0.15	0.95 ± 0.05
3750 H12	0.04 ± 0.02	0.04 ± 0.02	0.03 ± 0.02	<0.022	<0.027	<0.015	0.032± 0.004
3771 H11	0.04 ± 0.02	0.05 ± 0.01	0.02 ± 0.01	<0.018	<0.025	0.03 ± 0.01	0.041± 0.004
3798 H10	0.05 ± 0.02	0.06 ± 0.01	0.05 ± 0.01	0.07 ± 0.02	0.06 ± 0.02	0.06 ± 0.02	0.056± 0.004
3835 H9	0.07 ± 0.02	0.07 ± 0.01	0.07 ± 0.01	0.07 ± 0.01	0.07 ± 0.02	0.07 ± 0.01	0.074± 0.004
3865 [Ne III]	<0.012	0.03 ± 0.01	0.054 ± 0.008	0.60 ± 0.05	<0.011	0.029 ± 0.008	0.25±0.01
3889 H8+He I	0.17 ± 0.02	0.17 ± 0.02	0.20 ± 0.01	0.20 ± 0.02	0.14 ± 0.01	0.18 ± 0.02	0.201± 0.008
4026 He I	<0.008	0.010 ± 0.006	0.016 ± 0.005	0.018 ± 0.007	<0.009	0.016 ± 0.006	0.020 ± 0.002
4068 [S II]	<0.009	0.015 ± 0.007	0.010 ± 0.004	0.027 ± 0.008	0.020 ± 0.008	0.018 ± 0.005	0.015 ± 0.001
4100 Hδ	0.26 ± 0.02	0.26 ± 0.02	0.26 ± 0.01	0.26 ± 0.02	0.26 ± 0.02	0.26 ± 0.02	0.257 ± 0.009
4338 Hγ	0.47 ± 0.02	0.47 ± 0.02	0.47 ± 0.02	0.47 ± 0.03	0.47 ± 0.02	0.47 ± 0.03	0.47 ± 0.02
4363 [O III]	< 0.005	<0.005	<0.004	0.041 ± 0.006	<0.007	<0.004	0.022± 0.001
4471 He I	0.036 ± 0.006	0.035 ± 0.007	0.041 ± 0.005	0.047 ± 0.007	0.011 ± 0.006	0.031 ± 0.005	0.043 ± 0.002
4686 He II	<0.006	<0.007	<0.004	0.039±0.007	<0.005	<0.004	<0.001
4859 Hβ	1.00 ± 0.05	1.00 ± 0.04	1.00 ± 0.04	1.00 ± 0.05	1.00 ± 0.04	1.00 ± 0.05	1.00 ± 0.03
4959 [O III]	0.20 ± 0.02	0.27 ± 0.02	0.39 ± 0.02	2.16 ± 0.10	0.11 ± 0.01	0.28 ± 0.02	1.16±0.04
5007 [O III]	0.59 ± 0.04	0.78 ± 0.04	1.17 ± 0.06	6.60 ± 0.30	0.33 ± 0.02	0.83 ± 0.05	3.40±0.12
$C_{H\beta}$	0.12 ± 0.09	0.08 ± 0.08	0.32 ± 0.07	0.07 ± 0.10	0.41 ± 0.09	0.21 ± 0.09	0.01±0.04
EW (Å)	0.6	0.9	0.2	2.7	0.7	1.0	0.6

Table 3. Dereddened Line Fluxes with Uncertainties

Wavelength	BCLMP745	BCLMP705	BCLMP740	BCLMP706	BCLMP290A	MA1
3725 [O II]	0.87 ± 0.07	1.33 ± 0.11	1.22 ± 0.08	1.09 ± 0.12	0.89 ± 0.04	0.46 ± 0.03
3727 [O II]	1.26 ± 0.10	2.06 ± 0.17	1.73 ± 0.11	1.70 ± 0.17	1.34 ± 0.06	0.68 ± 0.05
3750 H12	0.04 ± 0.02	0.06 ± 0.01	0.03 ± 0.01	0.05 ± 0.02	0.042 ± 0.004	<0.016
3771 H11	0.05 ± 0.02	0.07 ± 0.01	0.05 ± 0.01	0.06 ± 0.02	0.046 ± 0.003	<0.014
3798 H10	0.05 ± 0.01	0.07 ± 0.01	0.06 ± 0.02	0.05 ± 0.02	0.057 ± 0.005	<0.016
3835 H9	0.07 ± 0.01	0.07 ± 0.02	0.074 ± 0.009	0.07 ± 0.02	0.074 ± 0.005	0.07 ± 0.01
3865 [Ne III]	0.08 ± 0.01	<0.013	0.056 ± 0.006	0.14 ± 0.02	0.084 ± 0.005	0.41 ± 0.02
3889 H8+He I	0.16 ± 0.02	0.17 ± 0.02	0.18 ± 0.01	0.21 ± 0.02	0.186 ± 0.008	0.16 ± 0.01
4026 He I	0.014 ± 0.005	<0.007	0.010 ± 0.004	0.022 ± 0.009	0.011 ± 0.002	<0.009
4068 [S II]	0.020 ± 0.005	0.021 ± 0.007	0.022 ± 0.004	0.017 ± 0.008	0.008 ± 0.002	<0.007
4100 Hδ	0.26 ± 0.02	0.26 ± 0.02	0.26 ± 0.01	0.26 ± 0.02	0.259 ± 0.009	0.25 ± 0.02
4338 Hγ	0.47 ± 0.03	0.47 ± 0.03	0.47 ± 0.02	0.47 ± 0.03	0.47 ± 0.02	0.48 ± 0.02
4363 [O III]	0.013 ± 0.004	<0.007	<0.004	0.012 ± 0.005	0.011 ± 0.002	0.043 ± 0.006
4471 He I	0.034 ± 0.005	0.020 ± 0.007	0.035 ± 0.004	0.040 ± 0.007	0.035 ± 0.002	0.016 ± 0.006
4686 He II	<0.003	<0.005	<0.003	<0.006	<0.001	0.049±0.004
4859 Hβ	1.00 ± 0.04	1.00 ± 0.05	1.00 ± 0.04	1.00 ± 0.05	1.00 ± 0.03	1.00 ± 0.03
4959 [O III]	0.58 ± 0.03	0.19 ± 0.02	0.44 ± 0.03	0.72 ± 0.07	0.61 ± 0.02	1.68 ± 0.06
5007 [O III]	1.70 ± 0.08	0.59 ± 0.05	1.30 ± 0.07	2.19 ± 0.14	1.88 ± 0.07	5.30 ± 0.20
$C_{H\beta}$	0.29 ± 0.09	-0.17 ± 0.10	0.13 ± 0.07	0.22 ± 0.11	-0.10 ± 0.05	0.01 ± 0.07
EW (Å)	1.5	1.8	0.6	1.2	0.7	0.6

Table 4. Measured Electron Temperatures and Densities

ID	T[O III] (K)	n_e (cm^{-3})
BCLMP016	...	< 180
BCLMP027	...	< 170
BCLMP094	...	< 210
BCLMP090	$9,900 \pm_{400}^{500}$	< 250
BCLMP696	...	< 160
CPDSP212	...	< 170
BCLMP691	$10,000 \pm_{200}^{200}$	100 ± 60
BCLMP745	$10,600 \pm_{600}^{1200}$	< 190
BCLMP705	...	< 130
BCLMP740	...	< 170
BCLMP706	$9,600 \pm_{600}^{1300}$	< 170
BCLMP290A	$9,800 \pm_{400}^{600}$	< 80
MA1	$10,800 \pm_{400}^{600}$	< 150

Table 5. Ionic and Elemental Abundances

ID	$O^+/H^+(\times 10^5)$	$O^{+2}/H^+(\times 10^5)$	$Ne^{+2}/H^+(\times 10^5)$	$\log(O/H)$	$\log(Ne/H)$
BCLMP090	7.6 ± 1.2	23.8 ± 3.9	6.8 ± 1.4	-3.50 ± 0.06	-4.04 ± 0.09
BCLMP691	6.3 ± 0.4	12.0 ± 0.7	2.7 ± 0.2	-3.74 ± 0.02	-4.38 ± 0.03
BCLMP745	6.8 ± 2.0	5.0 ± 1.7	0.7 ± 0.3	-3.93 ± 0.10	-4.8 ± 0.2
BCLMP706	12.0 ± 4.5	9.0 ± 3.9	1.9 ± 1.0	-3.68 ± 0.12	-4.4 ± 0.3
BCLMP290A	9.0 ± 1.5	7.2 ± 1.4	1.0 ± 0.2	-3.79 ± 0.06	-4.6 ± 0.1
MA1	3.4 ± 0.5	14.2 ± 2.2	3.3 ± 0.6	-3.76 ± 0.06	-4.39 ± 0.08

Table 6. Derived Galactocentric Raddi and Electron Temperatures for Vílchez et al. (1988) H II Regions

ID	Rad. (pc)	$T[S III]$ (K)	$T[O II]$ (K)	$T[O III]$ (K)
MA2	2033	...	$9,000 \pm_{700}^{1300}$...
NGC595	2846	$7,700 \pm_{400}^{600}$
NGC604	4066	...	$9,100 \pm_{200}^{300}$	$8,500 \pm_{200}^{300}$
IC131 (BCLMP290A)	4380	$9,500 \pm_{400}^{600}$
NGC588	6505	$9,300 \pm_{400}^{600}$

Table 7. Ionic and Elemental Abundances for Vílchez et al. (1988) H II Regions

ID	$O^+/H^+(\times 10^5)$	$O^{+2}/H^+(\times 10^5)$	$Ne^{+2}/H^+(\times 10^5)$	$\log(O/H)$	$\log(Ne/H)$
MA2	$11.2 \pm_{4.6}^{7.7}$	$10.8 \pm_{4.0}^{9.2}$	$2.0 \pm_{0.7}^{2.1}$	$-3.7 \pm_{0.1}^{0.2}$	$-4.4 \pm_{0.2}^{0.5}$
NGC595	$23.3 \pm_{7.8}^{10.6}$	$17.8 \pm_{5.3}^{7.5}$...	-3.4 ± 0.1	...
NGC604	12.1 ± 1.6	14.0 ± 1.9	2.5 ± 0.4	-3.58 ± 0.04	-4.33 ± 0.08
IC131 (BCLMP290A)	9.2 ± 1.6	16.6 ± 3.3	6.5 ± 1.9	-3.59 ± 0.06	-4.0 ± 0.1
NGC588	6.8 ± 1.3	21.2 ± 4.6	6.1 ± 1.6	-3.55 ± 0.07	-4.1 ± 0.1